

Ultrasound Autofocusing: Common Midpoint Phase Error Optimization via Differentiable Beamforming

Walter Simson,^{1,*} Louise Zhuang,^{2,*} Benjamin N. Frey,³ Sergio
J. Sanabria,^{1,4} Jeremy J. Dahl,^{1,†} and Dongwoon Hyun^{1,5}

¹*Department of Radiology, School of Medicine, Stanford University, Stanford, CA, 94305, USA*

²*Department of Electrical Engineering, Stanford University, Stanford, CA, 94305, USA*

³*Department of Applied Physics, Stanford University, Stanford, CA, 94305, USA*

⁴*Ikerbasque, Basque Foundation for Science, Bilbao, Spain*

⁵*Siemens Healthineers, Palo Alto, CA, 94304, USA*

(Dated: October 7, 2024)

Wavefield imaging reconstructs physical properties from wavefield measurements across an aperture, using modalities like radar, optics, sonar, seismic, and ultrasound imaging. Propagation of a wavefront from unknown sources through heterogeneous media causes phase aberrations that degrade the coherence of the wavefront leading to reduced image resolution and contrast. Adaptive imaging techniques attempt to correct phase aberration and restore coherence leading to improved focus. We propose an autofocusing paradigm for aberration correction in ultrasound imaging by fitting an acoustic velocity field to pressure measurements, via optimization of the common midpoint phase error (CMPE), using a straight-ray wave propagation model for beamforming in diffusely scattering media. We show that CMPE induced by heterogeneous acoustic velocity is a robust measure of phase aberration that can be used for acoustic autofocusing. CMPE is optimized iteratively using a differentiable beamforming approach to simultaneously improve the image focus while estimating the acoustic velocity field of the interrogated medium. The approach relies solely on wavefield measurements using a straight-ray integral solution of the two-way time-of-flight without explicit numerical time-stepping models of wave propagation. We demonstrate method performance through *in silico* simulations, *in vitro* phantom measurements, and *in vivo* mammalian models, showing practical applications in distributed aberration quantification, correction, and velocity estimation for medical ultrasound autofocusing.

Keywords: Ultrasound | Autofocusing | Differentiable computing

Coherent imaging systems reconstruct the physical properties of distant sources using phase-sensitive wavefield measurements, such as radio waves in radar, visible light in optics, or acoustic waves in sonar, seismic, and ultrasound imaging. The search for signal coherence given an underlying propagation model is the unifying principle that underpins these modalities. Discrepancies between an assumed phase propagation model and the true propagation result in *phase aberration*, a defocusing effect degrading the resolution and contrast of a coherent imaging system. Examples of phase aberration include the unmodeled refraction in the Earth's atmosphere which reduces the coherence length astronomical measurements of distant stars [1], and unmodeled tissue velocity in medical ultrasound which degrades images [2]. Phase aberration poses a fundamental challenge for wavefield imaging through heterogeneous media where the spatial distribution of the acoustic properties in the propagation domain is unknown.

Adaptive imaging finds use in astronomy, optics, and ultrasound to model, measure, and directly compen-

sate for observed phase aberration. Early adaptive imaging techniques developed in astronomy included the phase screen model of the earth's thin atmosphere where phase shifts were measured and corrected using deformable mirrors to improve deep space image focus [3]. Phase screen models have been adopted in ultrasound imaging, where phase (or time) shifts between neighboring aperture elements are measured and iteratively corrected to compensate for phase aberration [4, 5]. Although phase screens are reasonable models of thin aberrating media near the aperture, such as the Earth's atmosphere or a thin layer of subcutaneous fat, they do not accurately model distributed near-field phase aberration often encountered in medical ultrasound imaging [6–8]. Wave propagation through heterogeneous biological tissue with varying acoustic velocities results in spatially dependent phase aberration that accumulates over the wave's travel path. Phase aberration correction can be achieved by modifying the wave propagation model to better match the true propagation.

Acoustic full waveform inversion (FWI) uses wavefield measurements as the template to which a wave equation operator is fit to recover physical domain properties such as absorption, acoustic velocity, or density.

* Equal contribution.

† Correspondence email address: jjdahl@stanford.edu

However, FWI is ill-posed for non-smooth property distributions, nonconvex, and computationally intensive [9] and does not take advantage of far-field coherence patterns to regularize the inverse-problem. Alternatively, seismic focusing analysis imaging techniques such as migration velocity analysis (MVA) and wave equation migration velocity analysis (WEMVA) update only the wavefield velocity used in a propagation model to optimize the flatness of specular reflectors in seismic images [10, 11]. While MVA uses a straight-ray operator and WEMVA uses a linearized wave equation operator, both methods allow for reflection tomographic reconstruction of wave velocity given well-defined specular reflections. In medical ultrasound, where diffuse scattering is prevalent, reflection tomographic methods such as Computed Ultrasound Tomography in Echo-mode (CUTE) have been proposed to estimate spatially varying velocity distributions based on matrix inversion of a forward phase shift distribution model. [12–17]. These models require careful design of the excitation sources, wave propagation and model inversion. Recovered velocity distributions have been shown to reduce the effect of phase aberration using straight ray, Eikonal, and linear wave propagation models in ultrasound imaging [2, 16, 18].

In autofocusing, phase aberration correction is applied iteratively to improve focus quality. A reliable focusing measure with the following characteristics is required to perform autofocusing: it is suitable for diffuse targets, has a well-defined optimal value, and has minimal randomness, i.e., jitter. Many existing focusing criteria for pulse-echo ultrasound do not display these properties. The classic main lobe width of the point spread function (PSF) describes the imaging system resolution, but traditionally requires a point source in the field of view, which requires manual target selection and is not possible in diffuse scattering. Speckle brightness [19], defined as the coherent sum of a diffuse scatterer source, is maximized when ideally focused, but the optimal value is target-dependent and unbounded. The coherence factor (CF) [20, 21], defined as the square of the speckle brightness normalized by the incoherent signal sum, is bounded between 0 and 1, but the optimum value is also target-dependent. The optimal CF value under ideal focusing for incoherent sources (diffuse scattering) is $2/3$, while the optimal CF value for coherent sources is 1. The spatial focusing factor (F -factor) is the quotient of a measured common midpoint PSF over the ideal common midpoint PSF at a given location in space [22]. The F -factor relies on a model fit of an idealized PSF and Gaussian noise and requires a sufficiently sized isoplanatic patch. Lastly, phase (or time) shifts between neighboring elements [4] can be used on diffuse targets, but as we will show, contain jitter due to the stochasticity of incoherent sources.

In this work, we introduce common midpoint phase

error (CMPE), a focusing measure derived from first principles enabling deterministic focusing in diffusely scattering media. We demonstrate that CMPE is a robust quantitative *measure* of image focus which can be used to evaluate the spatial distribution of phase aberration. Since diffuse scattering can be modeled as an incoherent source [23], the van Cittert-Zernike (VCZ) theorem [23, 24] applies. It defines the mutual coherence of an incoherent source across a far-field aperture as the Fourier transform of the spatial distribution of the source intensity. Symmetries in the VCZ theorem allow the modulation term to fall from the coherence equation when measurement points are equidistant from the center axis, thereby maximizing correlation [24]. For a pulse-echo ultrasound imaging system, this symmetry requires that transmit and receive aperture pairs share a common midpoint (CM) (c.f. Eq. 7 and Eq. 8) [7, 20, 25–27].

We build on this symmetry to derive the CMPE, which allows for the direct spatial quantification of phase aberration in diffusely scattering media. We apply CMPE to ultrasound autofocusing and velocity estimation in diffuse media. To this end we *optimize* velocity distributions using differentiable beamforming, as introduced in [28–30]. We further find that autofocusing via CMPE optimization produces spatially resolved velocity estimates *in vivo* which have the potential to serve as a diagnostic biomarker. We base our evaluation on *in silico* simulations, *in vitro* phantom measurements, and *in vivo* mammalian models. We display the practicality of the proposed CMPE and its application in localization and quantification of phase aberration, velocity estimation, and autofocusing. The theoretical basis of the CMPE offers more general applicability of our method to other wavefield imaging modalities such as general acoustics, radar, seismology, and optics.

RESULTS

The pointwise phase shift between two common midpoint images, $P_1(\mathbf{x})$ and $P_2(\mathbf{x})$, at focus position $\mathbf{x} = [x, y, z]^T$ is the complex angle of their mutual coherence:

$$\Delta\phi_{12}(\mathbf{x}) = \angle \mathbb{E}[P_1(\mathbf{x}_f)P_2^*(\mathbf{x})]. \quad (1)$$

The CMPE is the expected magnitude of the phase shift (i.e. the “phase error”) pairwise between all images reconstructed with transmit and receive apertures sharing a *common midpoint* (see derivation, Sec. E):

$$\text{CMPE}(\mathbf{x}) = \mathbb{E}_{(P_1, P_2) \in \text{CM}} |\Delta\phi_{12}(\mathbf{x})|. \quad (2)$$

where CM denotes a common midpoint relationship. While the point-wise CMPE visualizes aberration spatially in an image, the mean value of CMPE (see Eq. 10) is used as a loss term for optimization.

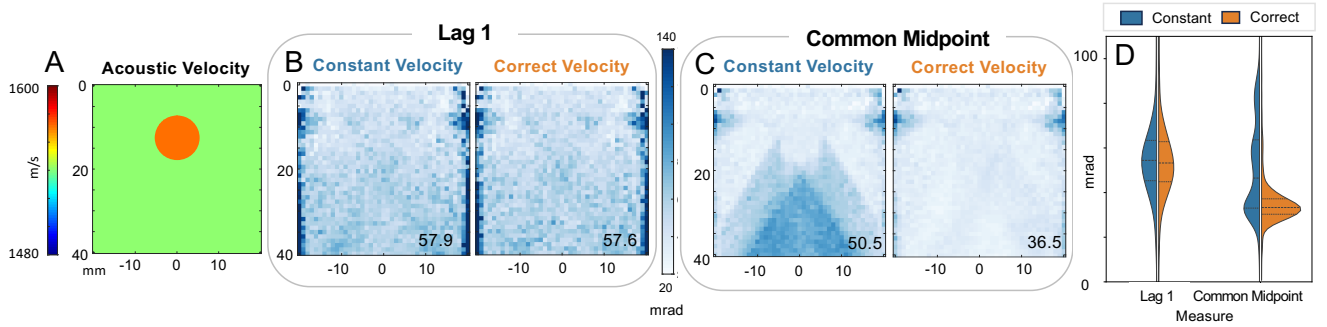


FIG. 1. (A) The true speed of sound for an *in silico* inclusion phantom used to simulate pulse-echo measurements for phase error evaluation. A comparison of phase error for a constant velocity reconstruction and the true velocity reconstruction is performed using (B) phase error with a lag-1 basis where the midpoint is offset by 1-element-width and (C) the CMPE basis where the midpoints coincide. (D) A comparison of the phase error distributions in the image between correct and incorrect velocity models for the lag-1 and common midpoint bases.

A. Common Midpoint Phase Error as a Focusing Measure

CMPE is first evaluated in known media by generating raw radio-frequency (RF) signals for every transmit-receive element combination (known as full-synthetic aperture, or FSA) using the k-Wave numerical solver of the Westervelt equation [31]. A heterogeneous velocity field containing a circular lesion of higher velocity is simulated as shown in Fig. 1A. The transmit and receive signals were retrospectively beamformed using N uniformly spaced and partially overlapping subapertures $\{T_1, T_2, \dots, T_N\}$ and $\{R_1, R_2, \dots, R_N\}$. We denote the image formed with the i -th transmit and j -th receive subaperture as $P_{i,j}(\mathbf{x})$.

Fig. 1B shows an image of the average phase error between $P_{i,j}(\mathbf{x})$ and $P_{i+1,j+1}(\mathbf{x})$, corresponding to subaperture pairs with a midpoint offset of 1 element (also called a lag 1 offset), for every spatial location in the medium. This phase error measurement is similar to the nearest-neighbor phase shift proposed in [4]. These aperture pairs do not share a common midpoint. Whether focusing with an incorrect assumption of constant velocity or with the correct velocity, the lag 1 phase error images do not qualitatively delineate the phase error. Also, the source of the underlying phase error is ambiguous; the phase error due to natural signal decorrelation from the midpoint shift between signals cannot be distinguished from the phase error due to the incorrect velocity assumption, making lag 1 phase error a poor measure of phase aberration.

In Fig. 1C, the CMPE is computed over all subaperture pairs sharing a common midpoint, e.g. $P_{i,j}(\mathbf{x})$ and $P_{i+1,j-1}(\mathbf{x})$ for every spatial location in the medium. According to the VCZ theorem, the CMPE should have an expected value of 0 mrad meaning that all error will be a result of an incorrect velocity assumption or prop-

agation model. In this work we focus on the constant velocity assumption. In Fig. 1C, the incorrect constant velocity assumption shows increased CMPE beneath the circular lesion, corresponding to the magnitude of the phase aberration induced by a mismatch between the assumption of a constant reconstruction velocity throughout the medium and the true velocity. Ultrasound image quality (e.g. resolution and contrast) is therefore expected to be worse in the darker regions of Fig. 1C with high CMPE. With the correct reconstruction velocity used for focusing, the CMPE behind the lesion disappears and the entire region shows a low and homogeneous CMPE, indicating an absence of phase aberration and that improved image focusing is applied. Unlike the lag 1 phase error, the CMPE image produces a spatially resolved measure of phase aberration strength.

We evaluate the information content of the two phase error measures by comparing their distributions before and after focusing in Fig. 1D, with mean phase errors annotated with the center dotted line of the respective distribution. The mean lag-1 phase error has a negligible change between incorrectly and correctly focused measurements (57.9 mrad to 57.6 mrad, $p = 0.72$). The mean CMPE is significantly improved (50.6 mrad to 36.5 mrad, $p < 0.001$) when a correct velocity model is applied for focusing. Fig. 1D further shows that the distribution of lag-1 phase error is nearly identical for constant and correct velocity focusing, as quantified by a Kullback-Leibler (KL) divergence of 0.035. Contrarily, CMPE displays a noticeable shift in distribution between the two focusing models, with a KL divergence of 1.16, showing that CMPE contains substantial phase aberration *information* not elucidated by the lag 1 phase error.

B. Autofocusing with CMPE Optimization

In beamforming, a simplified solution to the wave equation is used as an inverse model to assign received signals to their assumed spatial source. A constant velocity assumption leads to straight-ray model of wave propagation and time-of-flight values are calculated as the spatial integral $t_{e \rightarrow f} = \frac{1}{c} \int_{\mathbf{x}_e}^{\mathbf{x}_f} d\mathbf{x}$. Using the differentiable beamforming model proposed in [28], time-of-flight values are computed with a straight-ray propagation operator parameterized by the medium velocity $t_{e \rightarrow f} = \int_{\mathbf{x}_e}^{\mathbf{x}_f} \frac{1}{c(\mathbf{x})} d\mathbf{x}$. Here, the round-trip time-of-flight is computed as the straight-path integral of the slowness (i.e. inverse velocity) between the transmitter to the focal point and back to the receiver element. The slowness function is discretized into a grid and sampled along the rays via bi-linear interpolation of the nearest four slowness grid point to the ray sample location (c.f. Fig. 6). After a time-of-flight t is calculated, the respective channel data is sampled at t and the intensity is assigned to the focal point. Sub-images comprise spatial collections of focal points for transmit and receive pairs. Sub-images are consolidated by synthesizing larger sub-apertures, via superposition, to create sub-images of synthetic subaperture pairs also known as coherent compounding. CMPE (Eq. 10) can be calculated between sub-aperture image pairs that share a common midpoint. Importantly, the forward beamforming and CMPE models are formulated as compositions of differentiable operations allowing for calculation of the adjoint via automatic differentiation and back-propagation and optimization of the underlying velocity distribution via gradient descent [32–34]. In particular, we seek the optimal velocity distribution that minimizes CMPE given the straight-ray forward model. Differentiable beamforming allows the adjoint process to be calculated directly from the forward process and does not require separate forward process modeling as in model inversion methods [28].

Phantom experiment

Fig. 2 demonstrates autofocusing via CMPE minimization in a publicly available dataset [17] of a gelatin/silica phantom with heterogeneous acoustic velocity. The phantom comprises alcohol-gelatin inclusions near the surface to induce aberration relative to the background material. Two rows of copper wires (127 μm in diameter) serve as lateral resolution targets, and hypo-echoic cylindrical inclusions at the bottom of the phantom serve as contrast targets.

Fig. 2A shows B-mode image reconstruction using a global constant velocity of 1500 m/s, that minimizes CMPE. Fig. 2C shows an autofocused image of the same

data which displays hallmarks of improved focusing including tighter wire targets, brighter speckle, and tight and coherent specular menisci on the lower inclusions. The mean CMPE improves from 171 mrad before autofocusing to 81 mrad after CMPE autofocusing, corroborating the qualitative improvements. Enlarged insets of the wire targets in Fig. 2A and C are shown in each panel, respectively, to allow for easier comparison. Fig. 2B shows the lateral cross-sections of the wire targets from A and C, color-coded to their respective point annotations. Wire centers are established based on the maximum intensities of the reflection and overlaid on each other for comparison between the constant velocity (dotted) and CMPE autofocused (solid) images. The full-width half-maximum (FWHM) of the wire targets is shown in Fig. 2D. The average reduction in FWHM of the top row of wires is 107 μm , while the bottom row improved by 1528 μm on average. After CMPE autofocusing, the average FWHM over all wire targets is 182 μm , which is close to the theoretical diffraction limit of 148 μm .

In vivo experiment

Fig. 3 demonstrates CMPE autofocusing on *in vivo* data of Zucker rat models of metabolic-dysfunction associated liver disease [35]. The original images are reconstructed using a constant velocity (optimized to be 1570 m/s) and shown in Fig. 3 on the left under Original and the proposed CMPE autofocused images are shown on the right under Proposed.

Figs. 3A and 3C compare B-mode images before and after CMPE autofocusing. The CMPE autofocused image displays an overall brighter speckle and markedly tighter point features. Figs. 3E and 3G show magnified views of the region outlined by the yellow bounding box, highlighting the hepatic vein and surrounding liver structures. The CMPE autofocused image shows vessels with higher contrast, tighter boundaries and improved specular reflector definition. A video depicting CMPE autofocusing of this image is provided as supplementary material.

Figs. 3F and 3H show the receive channel data (i.e. axial sampling of the focused echo-wavefronts) corresponding to the green lines in the respective images. The CMPE autofocused channel data have a higher amplitude and more coherent wavefronts due to improved focusing. Figs. 3B and 3D, the CF of the receive channel data is plotted vertically in gray over the axial extent of the measurement. A 20-sample moving average is overlaid in light blue. After CMPE autofocusing, the CF is increased in Fig. 3C and D.

Figs. 3I and 3K show the spatial CMPE images throughout the field of view, where CMPE autofocusing is seen to reduce the CMPE, particularly near the

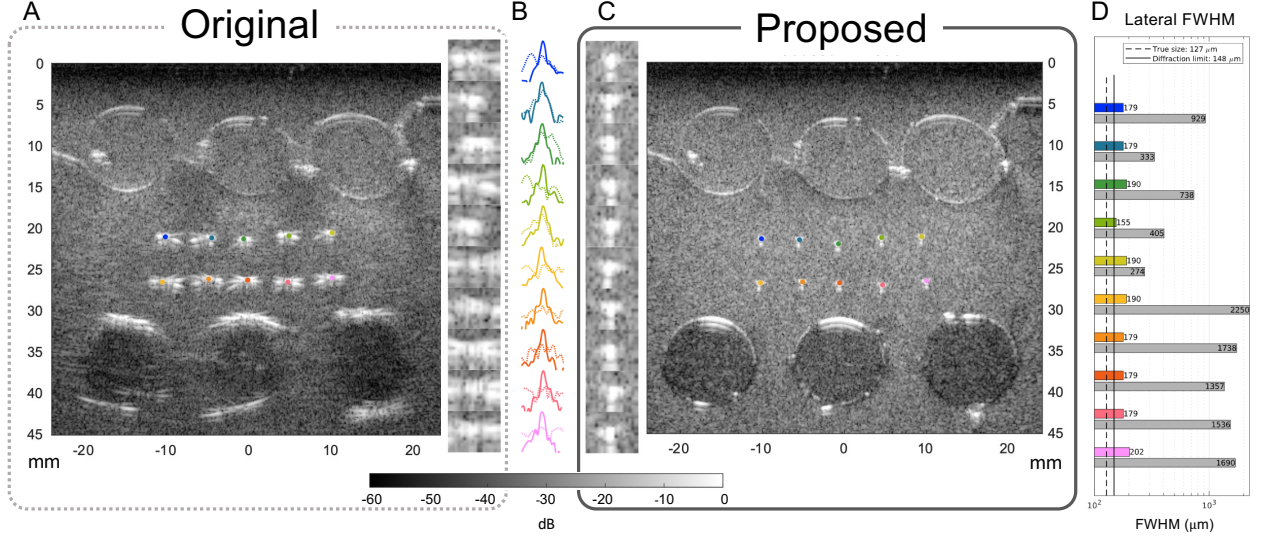


FIG. 2. (A) The resulting B-mode image of a tissue-mimicking phantom from Ali et al. [17] using a constant velocity (1500 m/s) reconstruction model. Both rows of cylindrical inclusions display geometric distortions. Below the top row of isoechoic inclusions, the image is severely aberrated. The wire targets are poorly resolved with energy spread over 5 mm laterally. The menisci on the lower row of inclusions are poorly focused. (B) The lateral cross-sections of the 10 wire targets within the phantom are annotated with corresponding colored points. Dotted lines are used for (A) and solid lines are used for (C). The cross-sections are normalized to the maximum value and displayed over a 50 dB of dynamic range and 2.5 mm width. (C) The resulting B-mode image after CMPE autofocus. The image appears brighter and more homogeneous, the menisci are focused well, and the geometrical distortion of the cylindrical inclusions is reduced. (D) The Full width at half maximum (FWHM) width of the wire targets from (A) & (C).

top and bottom left of the image. The speckle in these regions increases in brightness, indicating phase aberration correction. Quantitatively, the mean CMPE is reduced from 55.8 to 42.1 mrad after CMPE autofocus. Figs. 3J and 3L compare the signed phase shifts between pairs of common midpoint apertures that contribute to the mean CMPE, measured at the red point annotation, before and after autofocus. CMPE autofocus reduces the magnitude of the phase shift, indicated by a whiter appearance.

C. Velocity Reconstruction with CMPE Optimization

Fig. 4 shows *in vivo* velocity fields estimated by CMPE autofocus. In Telichko et al. [35], obese Zucker rats were fed a high-fat diet to induce steatosis, resulting in velocity variations in the liver. The left column displays example CMPE autofocused B-mode images from two of these rats, while the right column displays a velocity field estimate overlaid on the B-mode image. Fig. 4A shows the CMPE autofocused B-mode of two liver lobes layered vertically and delineated by a bright horizontal interface in the center of the B-mode image. The velocity used to focus the image is overlaid on the B-mode in Fig. 4B and shows a different

velocity in each lobe with good spatial agreement with the liver lobes. Unique velocities of ~ 1570 m/s for the top layer and ~ 1550 m/s for the bottom layer are identified, consistent with the measurements in Telichko et al. that showed that liver lobes in these rats presented with different velocities. These estimated velocities are also consistent with other liver velocities measured in healthy and steatotic liver [35, 36].

Fig. 4C also shows distinct anatomical regions of the rat abdomen. (The first 3 mm contained unstable velocity estimates, possibly due to natural phase errors from diffraction of the elevation lens.) The tip of the median lobe presents with a low velocity of ~ 1480 m/s in Fig. 4D, indicative of steatosis. The low-velocity region also shows good spatial agreement and lateral delineation compared to the anatomical layout in the B-mode image. Specifically, the velocity on the right side of the lobe transitions sharply from a low velocity to a high velocity in the neighboring lobe, following the curvature of the underlying anatomy well. Furthermore, the low-velocity region slowly transitions to a higher-velocity moving from right to left within the median lobe as it connects to the main hepatic body out of frame. In two further measurements of the same animal in different orientations, this anatomical region presents consistently low velocity when CMPE autofocus is applied, showing low velocity ~ 1480 m/s for the same

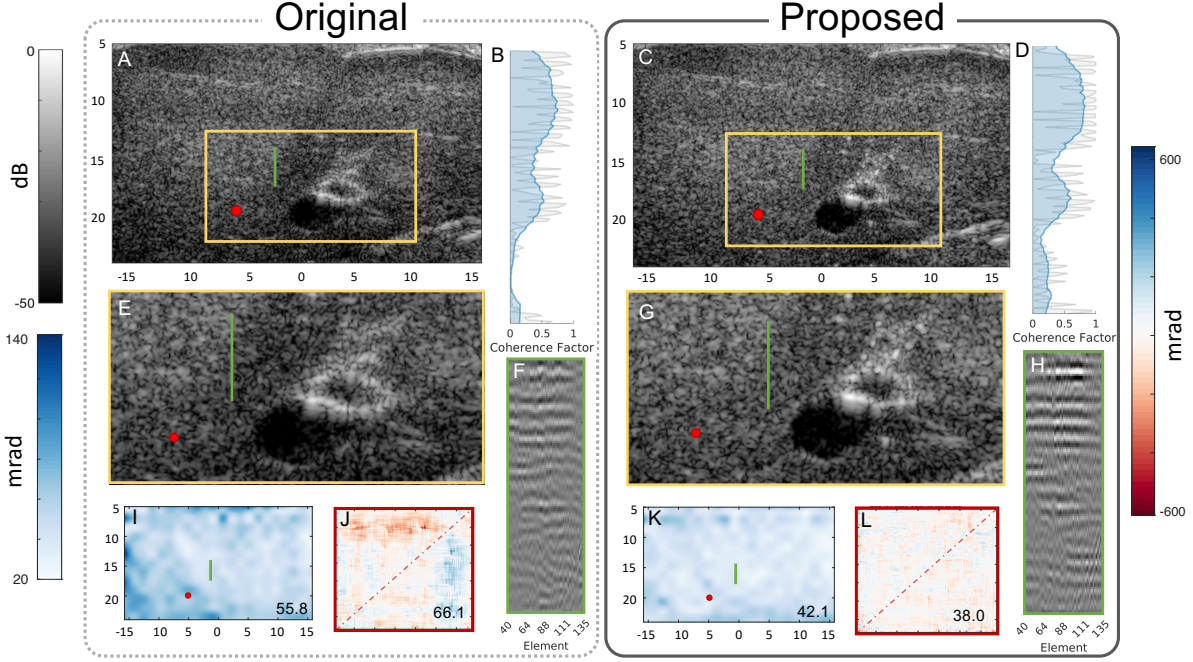


FIG. 3. In vivo example of CMPE autofocus. The original B-mode images (left) are created by constant acoustic velocity, and the proposed images (right) utilize CMPE autofocus. (A) & (C) B-mode images reconstructed using the two methods, with the regions marked by the yellow boxes magnified in (E) & (G). The CMPE is shown in (I) and (K) with the spatial average of the CMPE displayed in the lower right, in mrad. (J) & (L) Phase shifts between beamformed samples for all active transmit and receive sub-aperture-pairs for the location marked by the red dot in (A) & (E) and (C) & (G) respectively. Phase shifts measured above and below the dotted line should be symmetric due to acoustic reciprocity. The proposed method leads to an overall lower mean CMPE value annotated in mrad in the lower right of each sample i.e. the average of the magnitude of the phase shifts between tx/rx subaperture pairs. (B) & (D) The coherence factor (CF) of the channel data at the location of the green line in (A)&(E) and (C)&(G) respectively as a function of depth is shown as the gray line, with a 20-sample moving average shown in blue. The focused channel data on which the coherence factor is calculated is visualize in (F) and (H).

anatomical region (see supplemental material).

Additionally, the focusing quality of the CMPE autofocused *in vivo* B-mode images presented in Fig. 4 improved when the overlaid velocities were used in the reconstruction. The CMPE was reduced from 80.9 mrad to 63.5 mrad in the top row of B-mode images and from 84.6 mrad to 71.3 mrad in the bottom row of B-mode images. Videos of the iterative autofocus process can be found in the supplementary material.

DISCUSSION AND CONCLUSION

To measure focusing quality, we have introduced the CMPE as a reliable, robust measure that is applicable to diffuse scattering in heterogeneous media. Most focusing criteria are derived from the coherence of the wavefield across the receive aperture. Receive aperture coherence has been widely used to measure focusing quality and aberration in speckle, either via its phase shift [4], coherent sum magnitude [19], or other related quan-

ties [20]. However, the diffuse sub-resolution scatterers encountered in medical ultrasound imaging produce speckle, which exhibits only *partial* coherence across the receive aperture [23]. Speckle signals across the receive aperture increasingly decorrelate as their spacing increases at a rate predicted by the VCZT ((7), when $\Delta \mathbf{x}_t = 0$ but $\Delta \mathbf{x}_r \neq 0$). Speckle decorrelation manifests as phase shifts that are fundamentally indistinguishable from phase shifts caused by aberration, introducing uncertainty in phase shift estimation, or *jitter*, as quantified in (11). Fig. 1B demonstrates that jitter induced by speckle decorrelation can overwhelm the phase errors from aberration. For example, although ideal focusing is achieved under the correct velocity model, there is little or no change in the measured phase errors (57.6 mrad) compared to the incorrect velocity model (57.9 mrad), meaning that the measured phase errors in Fig. 1B are largely a product of speckle decorrelation and not aberration.

We have also demonstrated that the CMPE is an excellent objective function when using a differentiable

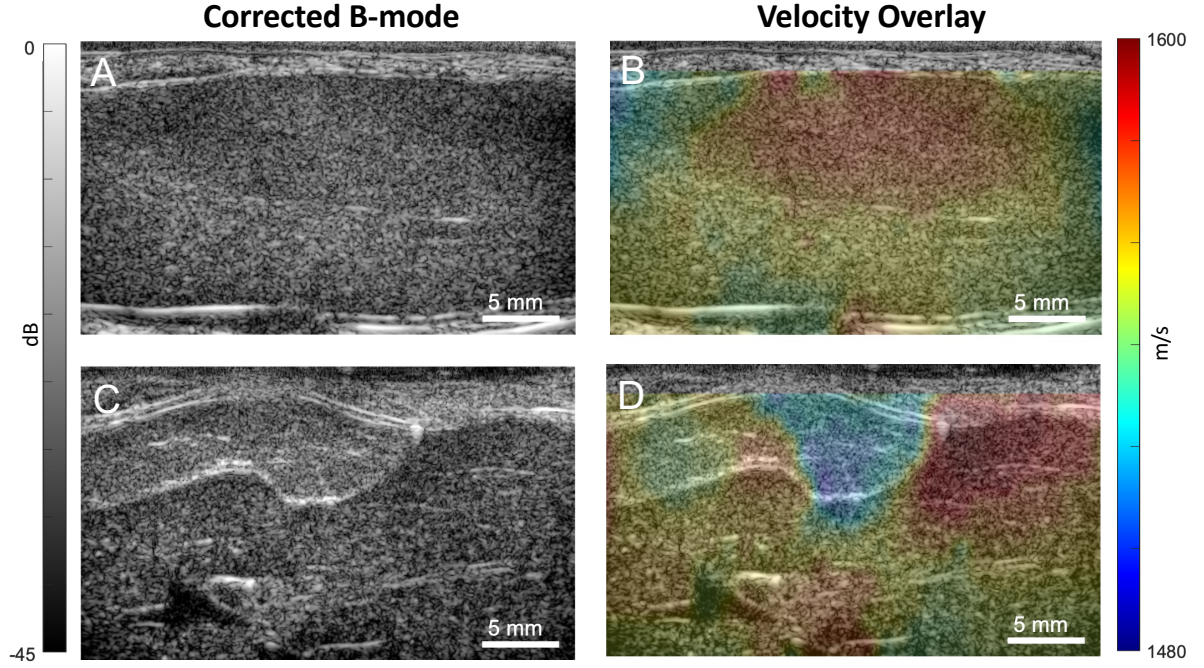


FIG. 4. Two examples of velocity estimation using CMPE on in vivo Zucker rat models of MASLD. (A) & (C) B-mode images of the livers in two different rats after CMPE autofocus. (B) & (D) show the velocity estimates overlaid on the CMPE autofocused B-mode image. These velocity estimates are used to parameterize the beamforming delays to optimally focus the B-mode image. The velocity estimates are spatially coherent and quantitatively plausible, with velocity values corresponding to biological tissue in literature. Spatial delineation in the velocity estimate also agrees with the underlying B-mode image. In the top row, images (A) & (B) show the right lateral lobe under the median lobe of the rat. The lobes are delineated by a bright interface visible in (A). This same pattern is seen in the velocity estimate in (B) where two distinct velocities distinguish the two lobes spatially. In the second row, (C) & (D) show the median lobe with higher echogenicity in the upper left with an estimated lower velocity than the other portions of the liver in the image. The spatial distribution of the velocity is highly correlated with the shape of the anatomy. The tip of the median lobe (top center) is delineated by a transition from a low velocity of ~ 1510 m/s to a higher velocity of ~ 1580 m/s.

beamforming model to achieve autofocus. Focusing measures based on receive aperture coherence are traditionally not maximized by correct focusing in diffusely scattering media, making them poor optimization objectives. For instance, one can artificially exceed the $CF = \frac{2}{3}$ expected of correct focusing in speckle [20] by overfitting to the jitter, thereby introducing artificial aberration into the focusing to produce false point targets. In contrast, common midpoint images of speckle are very highly correlated and have minimal jitter (combining (9) and (11)), allowing phase errors to be attributed almost entirely to aberration (Fig. 1). Prior phase aberration correction methods utilized an isoplanatic patch size when applying correction [2, 6, 37]. The isoplanatic patch size determines the rate at which the phase screen (i.e. the delays and advances of the wavefront across the focused aperture) changes with respect to translation of the beamformer's focal point. Reconstruction quality in these models is highly sensitive to the selected isoplanatic patch size, which acts as a regularizer to constrain the large solution space of phase

screens. However, we note that the actual isoplanatic patch size is a physical consequence of acoustic velocity variations. Our model instead parameterizes the beamformer as a function of the underlying speed of sound, such that isoplanatic patch size selection becomes unnecessary; it is implicitly enforced by the geometry of the velocity model. This parameterization naturally constrains the solution space of spatially-varying aberration laws to ones compatible with the physical model of medium velocity, and is observed to be capable of producing high focusing quality at all image locations.

A byproduct of our CMPE autofocus is the estimate of the underlying acoustic velocity. However, the velocity estimates used for CMPE aberration correction are optimized to minimize CMPE and not explicitly to faithfully model the underlying velocity field. The reflection tomographic velocity estimation problem is notoriously ill-posed and multiple velocity fields can lead to similar focus quality [10]. The limited aperture in pulse-echo imaging leads to insufficient angular sampling, leading to a challenging reconstruction prob-

lem for internal volume states as suggested by Kirchhoff's Integral Theorem [38]. Nevertheless, preliminary work *in silico* [28] suggests that CMPE autofocusing can lead to spatially and quantitatively accurate velocity estimates that can potentially be used as diagnostic biomarkers of tissue abnormality.

The biomarker potential of CMPE velocity estimates is highlighted in Fig. 4, where a lower velocity correlates with higher fat content and steatosis grading in the liver. The CMPE velocity estimates agree with prior estimations in these same rats [16, 35], but with a higher spatial resolution of velocity estimates. This improved velocity resolution not only leads to improved CMPE autofocusing, but also spatial variations in biomarker distribution. For example, in Telichko et al. [35], the separate lobes of the liver presented with different velocities, indicating that liver steatosis was not homogeneous across the organ. Fig. 4 shows that these differences across liver lobes can effectively be distinguished with the velocity estimates from CMPE autofocusing.

There are several sources of potential error that our beamforming model does not address. Our beamforming model employed the commonly used straight ray model of wave propagation, which ignores any refraction or wave-based diffraction effects. These effects can manifest as spurious CMPE, and may cause this model to break down in media with significant sound speed heterogeneity (e.g., transcranial imaging through the skull). At the same time, this specific error could be viewed as a confidence metric of the accuracy of a beamforming model, such as the straight ray model used here. For example, the straight ray model breaks down under strong diffracting elements or refracting layers, such as a checker-board phantom of acoustic velocity [28], can be identified by residual CMPE after CMPE autofocusing. Models accounting for the refraction and diffraction, such as those used in Ali et al. [16] or WEMVA [11] may produce less CMPE.

Similarly, thermal noise and reverberation clutter can manifest as spurious CMPE, especially in hypoechoic or anechoic targets. Historically aberration correction methods cannot accurately measure and correct aberration in these regions and may require methods to identify anechoic regions such as in Chau et al. [6] or assuming a constant velocity over the anechoic region, as is in Sanabria et al. [13]. Avoiding the computation of CMPE in anechoic regions would mitigate erroneous gradients in the back propagation step and improve reflection tomographic velocity reconstruction with differentiable beamforming.

Errors in aperture synthesis can manifest as CMPE, such as the effect of a limited physical aperture in virtual source models (e.g., plane or diverging wave synthetic transmit aperture), or inaccurate multistatic data recovery using spatially-coded apertures (e.g., the RE-FoCUS technique [39, 40]). Finally, the CMPE was

derived under the assumption of an incoherent source in a diffusely scattering media ((5)), and not for coherent sources like specular reflectors, though we note that there is prior work suggesting that the mutual coherence of a coherent source exhibits similarly ideal CMPE [7, 24]. Collectively, these sources of potential errors in CMPE manifested here as non-zero CMPE after optimization or when using the ground truth velocity, but did not prevent the optimization from achieving autofocusing.

CMPE autofocusing has far-reaching potential. Improved focusing quality may lead to more accurate anatomical measurements, fewer exams limited by body habitus, and improved contrast-enhanced applications like molecular imaging and super-resolution imaging. The velocity estimates recovered from CMPE autofocusing can be used to guide and monitor therapeutic applications, such as neuromodulation, microbubble-guided drug delivery, or high-intensity focused ultrasound. In the rapidly growing field of wearable ultrasound, CMPE autofocusing can be used to estimate the shape of a flexible array to help enable at-home longitudinal monitoring of health [29]. Differentiable beamforming can also be used to estimate probe trajectory to achieve freehand 3D swept synthetic aperture imaging and reduce operator dependence [30]. Being deeply rooted in statistical optics and automatic differentiation, CMPE autofocusing has broad applicability to any active wavefield imaging of diffusely scattering media wherein one or more reconstruction parameters are imprecisely known.

MATERIALS AND METHODS

D. Pulse-Echo Coherence

Assuming Fresnel (small angle) and Fraunhofer (far-field) approximations [41], the pulse-echo signal due to transmit aperture function T , scattering function S , and receive aperture function R can be written as:

$$P(T, S, R) \approx \frac{e^{j2kz}}{(4\pi k)^2} \int_{\Omega} \tilde{T}(\mathbf{x}) S(\mathbf{x}) \tilde{R}(\mathbf{x}) e^{jkz^{-1}\|\mathbf{x}\|} d\mathbf{x}, \quad (3)$$

where $k = 2\pi/\lambda$ is the wavenumber, z is the distance separating the aperture planes from the scattering plane Ω , and where \tilde{T} and \tilde{R} are spatial 2D Fourier transforms of the transmit and receive apertures (i.e. $\tilde{A}(\mathbf{x}) = \int_{\mathcal{A}} A(\mathbf{x}_a) \exp[-j\mathbf{x}^\top \mathbf{x}_a] d\mathbf{x}_a$). In this formulation, the transmit and receive functions are *focused*, or equivalently, in the far-field of the scattering plane, which is achieved in ultrasound imaging using beamforming.

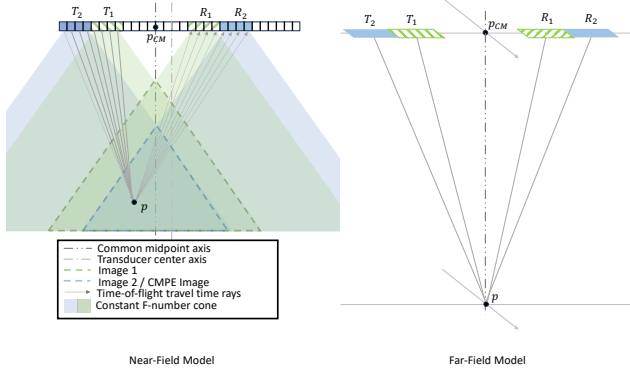


FIG. 5. (Left) The near-field ray based model for sub-aperture reconstruction of two common midpoint sub-apertures pairs (T_1/R_1) and (T_2/R_2) . Green and blue regions define the constant f -number masks of the sub-aperture pairs and thereby the valid image region in their respective unions signified by the triangles with dotted lines. The point p depicts a valid image reconstruction point, included in both sub-aperture pair images and thereby valid for CMPE calculation. Of note is that p is not by definition positioned under the common-midpoint p_{CM} on the aperture. (Right) The far-field model after far-field projection via beamforming. In the far field, the rays from the tx/rx apertures to p are of near equal length placing p on the common midpoint axis p_{CM} . This leads to near-perfect coherence of an incoherent source under the VCZ theorem.

The mutual coherence [24] of two pulse-echo signals (i.e. their complex correlation) can be written as

$$\Gamma_{12} = \mathbb{E} [P(T_1, S_1, R_1) P^*(T_2, S_2, R_2)], \quad (4)$$

where P^* denotes the complex conjugate of P . In biological tissue, the scattering is commonly modeled as diffuse and spatially incoherent, such that

$$\mathbb{E} [S_1(\mathbf{x}_1) S_2^*(\mathbf{x}_2)] = |S_0|^2 \delta(\mathbf{x}_1 - \mathbf{x}_2). \quad (5)$$

Under this model, the mutual coherence simplifies to

$$\Gamma_{12} \approx \frac{|S_0|^2}{(4\pi k)^4} \int_{\Omega} \tilde{T}_1(\mathbf{x}) \tilde{T}_2^*(\mathbf{x}) \tilde{R}_1(\mathbf{x}) \tilde{R}_2^*(\mathbf{x}) d\mathbf{x}. \quad (6)$$

This result generalizes the van Cittert-Zernike theorem [23, 24] to incorporate large receive apertures [42], and predicts that the coherence of arbitrary transmit-receive pairs (T_1, R_1) and (T_2, R_2) depends only on the aperture functions and not the spatially incoherent scattering function S .

E. The Common Midpoint Phase Error Measure

Consider the case of translating apertures [27], where $T_1(\mathbf{x}_t + \Delta\mathbf{x}_t) = T_2(\mathbf{x}_t) = T(\mathbf{x}_t)$ and $R_1(\mathbf{x}_r + \Delta\mathbf{x}_r) =$

$R_2(\mathbf{x}_r) = R(\mathbf{x}_r)$. Then, (6) further simplifies as

$$\Gamma_{12}^{\text{TA}} \approx \frac{|S_0|^2}{(4\pi k)^4} \int_{\Omega} |\tilde{T}(\mathbf{x})|^2 |\tilde{R}(\mathbf{x})|^2 e^{jkz^{-1}\mathbf{x}^\top(\Delta\mathbf{x}_t + \Delta\mathbf{x}_r)} d\mathbf{x}. \quad (7)$$

When $\Delta\mathbf{x}_t + \Delta\mathbf{x}_r = 0$, i.e., when (T_1, R_1) and (T_2, R_2) share a *common midpoint* (CM), the exponential term vanishes:

$$\Gamma_{12}^{\text{CM}} \approx \frac{|S_0|^2}{(4\pi k)^4} \int_{\Omega} |\tilde{T}(\mathbf{x})|^2 |\tilde{R}(\mathbf{x})|^2 d\mathbf{x}, \quad (8)$$

resulting in a real-valued mutual coherence with zero complex angle. Furthermore, the mutual coherence factor, which is defined as $\gamma_{12} = \Gamma_{12}/\sqrt{\Gamma_{11}\Gamma_{22}}$, becomes

$$\gamma_{12}^{\text{CM}} = \frac{\frac{|S_0|^2}{(4\pi k)^4} \int_{\Omega} |\tilde{T}(\mathbf{x})|^2 |\tilde{R}(\mathbf{x})|^2 d\mathbf{x}}{\sqrt{\left[\frac{|S_0|^2}{(4\pi k)^4} \int_{\Omega} |\tilde{T}(\mathbf{x})|^2 |\tilde{R}(\mathbf{x})|^2 d\mathbf{x} \right]^2}} = 1. \quad (9)$$

Two focused CM signals are expected to result in zero phase shift ($\angle\Gamma_{12}^{\text{CM}} = 0$) and ideal correlation coefficient ($\gamma_{12}^{\text{CM}} = 1$), even when the medium is composed of random, diffuse, spatially incoherent scatterers. Conversely, any measured nonzero phase shift is attributable to aberration or model errors, such as violations of the spatial incoherence assumption in (5).

Therefore, we measure the CMPE loss as the mean absolute phase shift deviation from zero over all pixels in the field of view:

$$\mathcal{L}_{\text{CMPE}} = \frac{1}{N_{\mathbf{x}} N_{\text{CM}}} \sum_{\mathbf{x}_f \in \text{FOV}} \sum_{(i,j) \in \text{CM}} |\angle\Gamma_{ij}(\mathbf{x}_f)|, \quad (10)$$

where $|\angle\Gamma_{ij}(\mathbf{x}_f)|$ denotes the phase error between CM signal pairs (i, j) focused at position \mathbf{x}_f . The CMPE quantifies the aberration and model error present in a given image. The estimation *jitter* of the phase-shift between any two speckle signals is given by [43]

$$\sigma_{\angle\Gamma}^2(\rho) = \frac{\pi^2}{3} - \pi \arcsin(\rho) + (\arcsin(\rho))^2 - \frac{1}{2} \text{Li}_2(\rho^2), \quad (11)$$

where $\rho = |\gamma_{12}|$ is the magnitude of the correlation coefficient. A remarkable consequence of CMP signals having ideal correlation ($\rho \approx 1$) is that the CMPE has zero expected jitter, i.e. $\sigma_{\angle\Gamma}^2(\rho) \approx 0$ for CMPE.

F. Optimizing Phase Error with Differentiable Beamforming

We formulate an adaptive image reconstruction method for focusing and image correction in diffuse

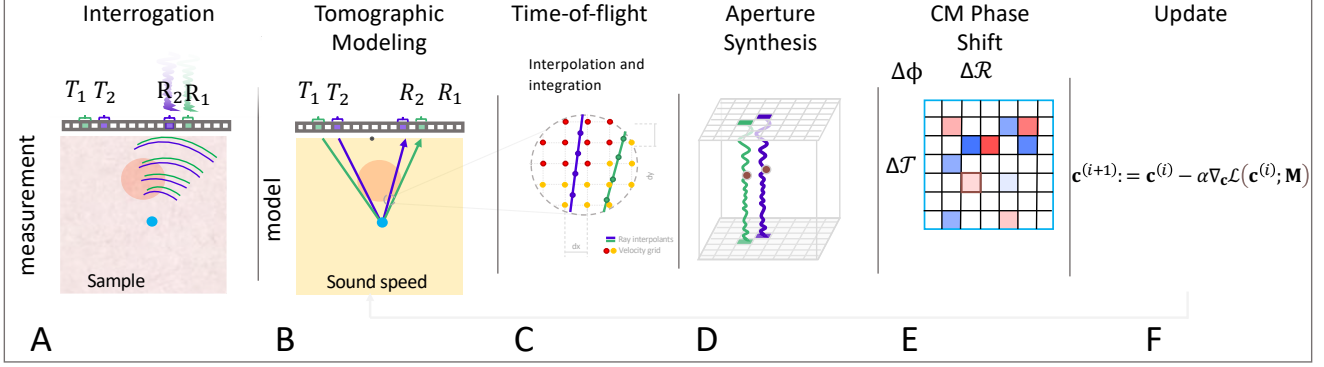


FIG. 6. The forward model used for ultrasound autofocus is presented above. (A) An acoustic measurement is taken by interrogating a sample with an acoustic wavefield and measuring the response. The measurement is performed between transmit aperture T and receive aperture R . (B) A time-of-flight model is derived from the ray-based reflection tomographic interrogation of an acoustic velocity field. The straight ray transmit and receive paths are modeled for a given point of interest (blue dot). (C) Acoustic velocity values along the ray are sampled via bi-linear interpolation for each ray path. (D) Transmit and receive pairs are combined to synthesize a larger transmit and receive apertures. (E) Phase error $\mathcal{L}_{\text{CMPE}}$ is calculated between transmit and receive aperture pairs with a common midpoint represented by red and blue entries in the measurements grid. (F) The phase the gradients CMPE are backpropagated through the forward process to the acoustic velocity field and a gradient decent update step is applied.

scattering media using a differentiable beamforming optimization pipeline [28]. We construct a differentiable imaging operator to focus wavefields from diffuse sources using the computational concept of auto-differentiation [44], which enables an efficient calculation of the adjoint [45, 46]. A set of single-sided FSA pressure measurements are collected as step one of the proposed method. Subaperture images are created for transmit and receive subapertures that share a common midpoint depicted in Fig. 6A. Subaperture pairs consisted of all 17-element subaperture combinations sharing a common midpoint. As seen in Fig. 6B, a reflection tomographic model is constructed to model the ray-based interrogation of the medium from the subaperture elements. To calculate the time of flight of the wave transmitted from \mathcal{T} focused at point p and reflection to the receive aperture \mathcal{R} , the velocities are interpolated bilinearly along the ray to calculate the travel time via numerical quadrature (Fig. 6C). The calculated travel time is used to sample the received channel data (delay) and synthesize an aperture (sum) (Fig. 6D). The synthesized aperture data is correlated with samples from other common midpoint pairs to measure the phase shift (Fig. 6E). Given a forward imaging operator and known correlation and modulation terms of signals received at symmetrical spatial locations, we assert that residual modulation of the complex correlation of two such images must come from an error in the time-delay model used in the imaging operator. A measured phase error in the correlation of beamformed signals is attributed to beamforming errors along the straight ray propagation path. When formulated as an optimization

loss the total CMPE is backpropagated through the forward model to update the velocity field (Fig. 6F). We perform these steps for all points in the imaging domain and all lag-1 common midpoint subaperture pairs. The optimization is performed until convergence. For the *in vivo* data, 100 steps of optimization are performed. For the *in silico* and *in vitro* phantom data 200 steps of optimization are performed.

Simulated Data

Simulated data used in the study is generated with k-Wave simulation suite [31] for the time-domain acoustic simulations. The phantom layouts display acoustic velocity variations shaped as inclusions for evaluation. Variations in the mean acoustic velocity of the medium are compensated by scaling the mean density with inverse proportionality to the acoustic velocity to achieve constant acoustic impedance. Diffuse reflections of sub-wavelength interfaces is held constant within the entire domain independent with modulation is performed in both the density and acoustic velocity of the medium. The transmit protocol is derived from [14], where plane wave transmits for comparison with the baseline method CUTE at angles of $\theta = \{-28.5^\circ : 0.5^\circ : 28.5^\circ\}$ are simulated. The recorded data is converted to the FSA basis using REFoCUS [37, 39, 40]. The simulated probe consists of 128 elements pitched 0.3mm apart. The probe has a center frequency of 4.8 MHz with 100% bandwidth and a one-cycle Gaussian-enveloped sinusoidal transmit pulse. All

transmissions are focused in the elevational dimension to 20 mm depth. The simulated 3D domain has dimensions of 60 mm \times 51 mm \times 7.4 mm.

Obese Zucker Rat Model

RF channel data from an obese Zucker rat (fa/fa, Charles River Laboratories Wilmington, MA, USA) fed a high-fat diet from the study in Telichko et al. [35] were used to evaluate the diagnostic usefulness of the proposed method. For visualization rats 18, 11 were used (top and bottom of Fig. 3 and rat 10 was used for visualization in 4. Briefly, these data were collected

from a research ultrasound scanner (Vantage 256, Verasonics Inc., Kirkland, WA, USA) using a linear array transducer (L12-3v, Verasonics Inc.). On transmit a Hadamard sequence was employed at a transmit frequency of 7.8 MHz negating the need to REFoCUS the data.

ACKNOWLEDGMENTS

This work was supported in part by the National Institute of Biomedical Imaging and Bioengineering under Grants R01-EB027100 and K99-EB032230.

-
- [1] R. Wilson and C. Jenkins, Monthly Notices of the Royal Astronomical Society **278**, 39 (1996).
 - [2] R. Ali, T. Brevett, L. Zhuang, H. Bendjador, A. S. Podkova, S. S. Hsieh, W. Simson, S. J. Sanabria, C. D. Herickhoff, and J. J. Dahl, *Zeitschrift für Medizinische Physik* **33**, 267 (2023), special Issue: Recent Advances in Ultrasound Imaging.
 - [3] J. M. Beckers, Annual review of astronomy and astrophysics **31**, 13 (1993).
 - [4] S. Flax and M. O'Donnell, IEEE Transactions on Ultrasonics, Ferroelectrics, and Frequency Control **35**, 758 (1988).
 - [5] M. O'Donnell and S. Flax, Ultrasonic Imaging **10**, 1 (1988).
 - [6] G. Chau, M. Jakovljevic, R. Lavarello, and J. Dahl, Ultrasonic imaging **41**, 3 (2019).
 - [7] D. Rachlin, The Journal of the Acoustical Society of America **88**, 191 (1990).
 - [8] A. Wild, R. Hobbs, and L. Frenje, Physics of the Earth and Planetary Interiors **120**, 219 (2000).
 - [9] J. Virieux and S. Operto, Geophysics **74**, WCC1 (2009).
 - [10] B. L. Biondi, *3D seismic imaging* (Society of Exploration Geophysicists, 2006).
 - [11] P. Sava and B. Biondi, Geophysical Prospecting **52**, 593 (2004).
 - [12] M. Jaeger, G. Held, S. Peeters, S. Preisser, M. Grünig, and M. Frenz, Ultrasound in medicine & biology **41**, 235 (2015).
 - [13] S. J. Sanabria, E. Ozkan, M. Rominger, and O. Goksel, Physics in Medicine & Biology **63**, 215015 (2018).
 - [14] P. Stähli, M. Kuriakose, M. Frenz, and M. Jaeger, Ultrasonics **108**, 106168 (2020).
 - [15] C. D. Bezek and O. Goksel, Ultrasonics, 107069 (2023).
 - [16] R. Ali, T. Brevett, D. Hyun, L. L. Brickson, and J. J. Dahl, IEEE transactions on ultrasonics, ferroelectrics, and frequency control **69**, 1714 (2022).
 - [17] R. Ali, T. M. Mitcham, M. Singh, M. M. Doyley, R. R. Bouchard, J. J. Dahl, and N. Duric, IEEE Transactions on Computational Imaging **9**, 367 (2023).
 - [18] R. Rau, D. Schweizer, V. Vishnevskiy, and O. Goksel, in *2019 IEEE International Ultrasonics Symposium (IUS)* (IEEE, 2019) pp. 2003–2006.
 - [19] L. Nock, G. E. Trahey, and S. W. Smith, The Journal of the Acoustical Society of America **85**, 1819 (1989).
 - [20] R. Mallart and M. Fink, The Journal of the Acoustical Society of America **96**, 3721 (1994).
 - [21] K. Hollman, K. Rigby, and M. O'donnell, in *1999 IEEE Ultrasonics Symposium. Proceedings. International Symposium (Cat. No. 99CH37027)*, Vol. 2 (IEEE, 1999) pp. 1257–1260.
 - [22] W. Lambert, J. Robin, L. A. Cobus, M. Fink, and A. Aubry, IEEE Transactions on Medical Imaging **41**, 3907 (2022).
 - [23] R. Mallart and M. Fink, The Journal of the Acoustical Society of America **90**, 2718 (1991).
 - [24] J. W. Goodman, *Statistical optics* (John Wiley & Sons, 2015).
 - [25] E. Larose, L. Margerin, A. Derode, B. van Tiggelen, M. Campillo, N. Shapiro, A. Paul, L. Stehly, and M. Tanter, Geophysics **71**, SI11 (2006).
 - [26] G. Ng, W. Walker, and G. Trahey, in *1996 IEEE Ultrasonics Symposium. Proceedings*, Vol. 2 (IEEE, 1996) pp. 1395–1400.
 - [27] G. C. Ng, P. D. Freiburger, W. F. Walker, and G. E. Trahey, IEEE transactions on ultrasonics, ferroelectrics, and frequency control **44**, 140 (1997).
 - [28] W. Simson, L. Zhuang, S. J. Sanabria, N. Antil, J. J. Dahl, and D. Hyun, in *International Conference on Medical Image Computing and Computer-Assisted Intervention* (Springer, 2023) pp. 428–437.
 - [29] D. Hyun, S. V. Narayan, W. Simson, L. L. Zhuang, and J. J. Dahl, in *2023 IEEE International Ultrasonics Symposium (IUS)* (IEEE, 2023) pp. 1–4.
 - [30] D. Hyun, in *2023 IEEE International Ultrasonics Symposium (IUS)* (IEEE, 2023) pp. 1–4.
 - [31] B. E. Treeby and B. T. Cox, Journal of biomedical optics **15**, 021314 (2010).
 - [32] H. J. Kelley, in *Mathematics in Science and Engineering*, Vol. 5 (Elsevier, 1962) pp. 205–254.
 - [33] D. E. Rumelhart, G. E. Hinton, and R. J. Williams, nature **323**, 533 (1986).

- [34] J. Bradbury, R. Frostig, P. Hawkins, M. J. Johnson, C. Leary, D. Maclaurin, G. Necula, A. Paszke, J. VanderPlas, S. Wanderman-Milne, and Q. Zhang, “JAX: composable transformations of Python+NumPy programs,” (2018).
- [35] A. V. Telichko, R. Ali, T. Brevett, H. Wang, J. G. Vilches-Moure, S. U. Kumar, R. Paulmurugan, and J. J. Dahl, *Physics in Medicine & Biology* **67**, 015007 (2022).
- [36] K. Tervola, M. Gummer, J. Erdman Jr, and W. O’Brien Jr, *The Journal of the Acoustical Society of America* **77**, 307 (1985).
- [37] W. Lambert, L. A. Cobus, T. Frappart, M. Fink, and A. Aubry, *Proceedings of the National Academy of Sciences* **117**, 14645 (2020).
- [38] W. A. Schneider, *Geophysics* **43**, 49 (1978).
- [39] N. Bottenus, *IEEE transactions on ultrasonics, ferroelectrics, and frequency control* **65**, 30 (2017).
- [40] R. Ali, C. D. Herickhoff, D. Hyun, J. J. Dahl, and N. Bottenus, *IEEE transactions on ultrasonics, ferroelectrics, and frequency control* **67**, 943 (2019).
- [41] J. W. Goodman, *Introduction to Fourier optics* (Roberts and Company publishers, 2005).
- [42] W. F. Walker and G. E. Trahey, *The Journal of the Acoustical Society of America* **101**, 1847 (1997).
- [43] J. W. Goodman, *Speckle Phenomena in Optics: Theory and Applications*, 2nd ed. (SPIE, 2020).
- [44] A. Griewank and A. Walther, *Evaluating derivatives: principles and techniques of algorithmic differentiation* (SIAM, 2008).
- [45] M. B. Giles and N. A. Pierce, *Flow, turbulence and combustion* **65**, 393 (2000).
- [46] W. Zhu, K. Xu, E. Darve, and G. C. Beroza, *Computers & Geosciences* **151**, 104751 (2021).